Original Article

Spiral time-of-flight magnetic resonance angiography for intracranial vascular imaging: performance compared to conventional Cartesian angiogram

Lina Xu[1,2]^, Jian Wu[3,4]^, Taishan Kang[5,6]^, Liangjie Lin[7]^, Shaomao Lv[5], Jianzhong Lin[5,6], Zhipeng Feng[5], Congbo Cai[2]^, Zhong Chen[2]^

[1]Medical Imaging Technology Section, Department of Computer Science, Jiangxi University of Chinese Medicine, Nanchang, China; [2]Fujian Provincial Key Laboratory of Plasma and Magnetic Resonance, Department of Electronic Science, Xiamen University, Xiamen, China; [3]Athinoula A. Martinos Center for Biomedical Imaging, Massachusetts General Hospital, Charlestown, MA, USA; [4]Department of Radiology, Harvard Medical School, Boston, MA, USA; [5]Department of MRI, Zhongshan Hospital of Xiamen University, School of Medicine, Xiamen University, Xiamen, China; [6]Xiamen Radiological Control Center, Xiamen, China; [7]MSC Clinical & Technical Solutions, Philips Healthcare, Beijing, China

Contributions: (I) Conception and design: T Kang, L Lin, J Wu, L Xu; (II) Administrative support: J Lin, C Cai, Z Chen; (III) Provision of study materials or patients: T Kang, J Lin; (IV) Collection and assembly of data: T Kang, S Lv, Z Feng; (V) Data analysis and interpretation: L Xu, J Wu; (VI) Manuscript writing: All authors; (VII) Final approval of manuscript: All authors.

Correspondence to: Taishan Kang, BS. Department of MRI, Zhongshan Hospital of Xiamen University, School of Medicine, Xiamen University, 201–209 Hubinnan Road, Xiamen 361004, China; Xiamen Radiological Control Center, Xiamen, China. Email: kkttss@126.com.

Background: Computed tomography angiography (CTA) and digital subtraction angiography (DSA) usually raise the risk of potential malignancies with cumulative radiation doses. Current time-of-flight magnetic resonance angiography (TOF-MRA) (dubbed as cTOF), which is based on Cartesian sampling mode, may show limited diagnostic conspicuity at sinuous or branching regions. It is also prone to relatively high false positive diagnoses and undesirable display of distal intracranial vessels. This study aimed to use spiral TOF-MRA (sTOF) as a noninvasive alternative to explore possible improvement, such that the application of magnetic resonance angiography (MRA) can be extended to facilitate clinical examination or cerebrovascular disease diagnosis and follow-up studies.

Methods: Initially, 37 patients with symptoms of dizziness or transient ischemic attack were consecutively recruited for suspected intracranial vascular disease examination from Zhongshan Hospital of Xiamen University between July 2020 and April 2021 in this cross-sectional prospective study. After excluding 1 patient with severe scanning artifacts, 1 patient whose scanning scope did not meet the requirement, and 1 patient with confounding tumor lesions, a total of 34 participants were included according to the inclusion and exclusion criteria. Each participant underwent intracranial vascular imaging with both sTOF and cTOF sequences on a 3.0 T MR scanner with a conventional head-neck coil of 16 channels. Contrast CTA or DSA was also performed for 15 patients showing pathology. Qualitative comparisons in terms of image quality and diagnostic efficacy ratings, quantitative comparisons in terms of signal-to-noise ratio (SNR), contrast-to-noise ratio (CNR), vessel length, and sharpness were evaluated. Pair-wise Wilcoxon test was performed to evaluate the imaging quality derived from cTOF and sTOF acquisitions and weighted Cohen's Kappa was conducted to assess the rating consistency between different physicians.

Results: Compared to cTOF, sTOF showed better performance with fewer artifacts. It can effectively alleviate false positives of normal vessels being misdiagnosed as aneurysm or stenosis. Improved conspicuity

^ ORCID: Lina Xu, 0000-0001-7600-9579; Jian Wu, 0000-0003-1445-2799; Taishan Kang, 0000-0002-0507-5525; Liangjie Lin, 0000-0002-3174-3136; Congbo Cai, 0000-0002-0600-8594; Zhong Chen, 0000-0002-1473-2224.

was observed in cerebral distal regions with more clearly identifiable vasculature at finer scales. Quantitative comparisons in selected regions revealed significant improvement of sTOF in SNR ($P<0.01$ or $P<0.001$), CNR ($P<0.001$), vessel length ($P<0.001$), and sharpness ($P<0.001$) as compared to cTOF. Besides, sTOF can depict details of M1 and M2 segments of middle cerebral artery (MCA) at metallic implant region, showing its resistance to magnetic susceptibility.

Conclusions: The sTOF shows higher imaging quality and lesion detectability with reduced artifacts and false positives, representing a potentially feasible surrogate in intracranial vascular imaging for future clinic routines.

Keywords: Spiral; time-of-flight magnetic resonance angiography (TOF-MRA); aneurysm; stenosis; intracranial vasculature

Submitted Oct 31, 2023. Accepted for publication Mar 14, 2024. Published online Apr 23, 2024.
doi: 10.21037/qims-23-1533
View this article at: https://dx.doi.org/10.21037/qims-23-1533

Introduction

The abnormal formation of intracranial vasculatures impedes blood-oxygen/nutrient supply and hemodynamic functionality, affecting brain parenchyma amid arteries and veins of all scales (1-3). Cerebrovascular diseases, such as ischemic and hemorrhagic stroke-related morbidities, have become the leading cause of brain impairment and functional loss (4-7).

Screening and characterization of cerebrovascular etiologies typically rely on intracranial vessel imaging. Computed tomography angiography (CTA) and digital subtraction angiography (DSA) are commonly used modalities, of which the former is suitable for fast imaging in acute brain pathology scenarios, and the latter can simultaneously enable sufficient spatial temporal resolution, whereas both modalities raise the stake of exposure to iodinated ion radiation (8,9). A recent follow-up study, involving 1 million children, adolescents, and young adults younger than 22 years old, revealed an association between cumulative computed tomography (CT) dose and risk of developing all hematological malignancies (10). Other limitations associated with the gold standard DSA include its invasive intervention, which increases the chance of thromboembolism or nephrotoxicity, and a risk of up to 2.6% for intracranial hemorrhage alone (11-13).

In the series of magnetic resonance angiography (MRA), contrast-enhanced MRA (CE-MRA) illuminates vessel lumen via gadolinium-enhanced imaging similar to CTA, which requires precise tracking of bolus arrival time (14,15). The phase-contrast MRA (PC-MRA) encodes endovascular flow rate and utilizes the phase shift to derive image contrast, a procedure highly dependent on specific flow rate and direction (16,17). Arterial spin labeling MRA (ASL-MRA), which labels the proton spins in arterial blood and uses them as endogenous agents, has shown its flexibility to depict large and middle-sized arteries compared to that of dynamic CE-MRA, but it usually requires long scan duration, with limited signal-to-noise ratio (SNR) or spatial resolution. Meanwhile, 3-dimensional (3D) time-of-flight MRA (TOF-MRA) has evolved to gain increased application, which utilizes inflow enhancement effect and is less affected by the variation of flow directions (18,19). Conventional Cartesian-based TOF-MRA (cTOF) that uses fast field echo sequence offers high SNR at a short acquisition time. It is however prone to signal loss and saturation effect caused by the stenosis of blood vessels or complex blood flow that inevitably fluctuates the bloodstream within the pixel. The susceptibility to image artifacts and motion-induced imperfections has incurred much inconvenience for clinical diagnosis. In particular, cTOF has been limited by a high false positive rate in misdiagnosing normal vessels as stenosis or aneurysm (20-24).

Besides the aforementioned TOF-MRA techniques, another continually evolved variant has been associated with spiral TOF-MRA (sTOF), which acquires data with spiral trajectories featuring densely sampled central region and sparsely sampled periphery. It allows for a much shorter echo time and a more effective *k*-space trajectory with flexible readout window, and it is inherently robust to motion and flow artifacts (25). Recent studies have applied spiral imaging to TOF-MRA, which emphasized the equivalent imaging quality spiral MRA could obtain and showed its comparable performance to cTOF (26-32).

The false positive challenge of cTOF and the versatile advantages of sTOF in cerebrovascular MRA have so far not been thoroughly examined. In effect, the superior imaging capability of sTOF in comparison to cTOF is beginning to emerge.

The purpose of this study was to evaluate the imaging quality of sTOF and its efficacy in alleviating false positive diagnoses of intracranial vascular diseases, exploring potential advantages that would not be readily achievable in cTOF. Furthermore, we also illustrate the feasibility of employing spiral cerebrovascular imaging as an alternative to conventional Cartesian imaging for future cerebral TOF-MRA acquisition. It is expected to improve MRA imaging quality and physicians' diagnostic confidence, in particular, to meet the increased demands of non-radioactive and noninvasive examination in clinical practice. We present this article in accordance with the STROBE reporting checklist (available at https://qims.amegroups.com/article/view/10.21037/qims-23-1533/rc).

Methods

Study setting

Patients with symptoms of dizziness or transient ischemic attack were consecutively recruited for suspected intracranial vascular disease examination between July 2020 and April 2021 at Zhongshan Hospital of Xiamen University. All participants provided written informed consent. The study was carried out in accordance with the Declaration of Helsinki (as revised in 2013). The study protocol was approved by the Institutional Review Board of Zhongshan Hospital of Xiamen University (No. xmzsyyky[2019019]).

As a prospective, single-center cross-sectional study, data eligible for selection fulfilled the following main inclusion criteria: (I) adult patients (age, ≥18 years), considering our prospective investigation involved an extended scan duration that may have become intolerable for children or adolescents; (II) acquisition of conventional T1, T2, and diffusion-weighted imaging (DWI) data prior to TOF-MRA imaging of both cTOF and sTOF sequences; (III) availability of CTA or DSA after TOF-MRA for diagnostically confirmed patients; (IV) a complete diagnostic report regarding intracranial vascular disease. The exclusion criteria were as follows: (I) artifacts caused by any subjective or objective factors such as motion that severely degenerate the acquired image to be justifiably evaluated; (II) the scanning field of view (FOV) did not fully cover our region of interest (ROI); (III) patients with acute, dangerous, severe disease onsets or confounding preexisting conditions other than cerebrovascular diseases (such as tumor in brain parenchyma).

Imaging acquisition

Patients assuming a head-first supine position underwent TOF-MRA with standard 3.0 T MR clinical scanner (Ingenia CX; Philips Healthcare, Best, the Netherlands) using 16 channels of a conventional head/neck coil. Prior to acquisition, the FOV was selected by positioning the circle of Willis of each participant to the center, with appropriate angle by adjusting the plane between the nasion and foramen magnum. Specifically, the FOV covered the internal carotid artery (ICA), distal vertebral artery (VA) and basilar artery (BA), anterior cerebral artery (ACA), middle cerebral artery (MCA), and posterior cerebral artery (PCA).

The 3D TOF-MRA data were collected following 2 imaging sequences. The cTOF refers to data acquisition using conventional Cartesian *k*-space readout, in which sensitivity encoding (SENSE) (33) was used with multiple receiver coils to accelerate the imaging procedure. Then, the k-space data of sTOF were obtained with the center-out spiral trajectory. Built-in software was used to calculate 2 maximum intensity projections (MIPs) to derive an angiogram. The cTOF parameters were selected directly following our institutional routine protocol; the sTOF parameters were chosen according to the vendor's recommendation and practical trials. The main acquisition parameters of both sequences are summarized in *Table 1*.

Imaging analysis and statistical evaluation

Qualitative image assessment according to different vessel segments was performed independently by 2 radiologists (≥10 years' experience) with 5-point Likert scales in a blinded manner, which were scored as 1, unacceptable image signals, bad vascular boundary, diagnosis very uncertain; 2, mild image quality, vague vascular boundary, diagnosis uncertain; 3, moderate image quality, weak lumen signals, diagnosis possible; 4, good image quality, good background suppression, diagnosis certain; 5, very good quality, good details, diagnosis strongly confirmed. For quantitative evaluation, the apparent SNR, apparent contrast-to-noise ratio (CNR), vessel length, and sharpness of the vessel lumen were calculated. The average signal

Table 1 Acquisition parameters of different sequences

Parameters	cTOF	sTOF
Acquisition duration	3 min 44 s	3 min 40 s
Tone	Yes, starting angle 16.2°	Yes, starting angle 16.2°
Flip angle (°)	18	18
TR (ms)	19	19
TE (ms)	3.45	3.45 (out phase)
FOV	200×188×120	180×180×120
Resolution (mm^3)	0.8×0.8×1.2	0.8×0.8×1.2
Slice number	200	200
SENSE factor	3	–
Chunks	4	4
Acquisition window (ms)	–	4
Receiver bandwidth (Hz/pixel)	108.8	–
Spiral interleaves	–	59
Flow compensation	Yes	Yes

The dash indicates there was no corresponding value for a given sequence. cTOF, Cartesian-based time of flight magnetic resonance imaging; sTOF, spiral-based time of flight magnetic resonance imaging; TR, repetition time; TE, echo time; FOV, field of view; SENSE, SENSitivity Encoding.

intensity (SI) was derived along the centerline of the vessel lumen with identically user-specified circular ROI (area ≥75% of the vascular cross section) on Philips postprocessing platform. Apparent SNRs were calculated as: $\mathrm{SNR}=10\times\log_{10}\left(\frac{SI_{mean}}{SD}\right)$, where SI_{mean} is the mean SI within the ROI and standard deviation (SD) is the standard deviation of the noise in the background region of the same slice. The apparent vessel to background CNRs were calculated as $CNR=\frac{SI_{vessel}-SI_{background}}{SD}$, where SI_{vessel} is the mean SI within the selected vessel, $SI_{background}$ is the mean SI of the surrounding tissue, and SD is the standard deviation of the noise in the background region of the same slice. Vessel detection was performed on the original image prior to the calculation of vessel length and sharpness. The vessel length was obtained by skeletonizing the vessel and counting the pixel number using MATLAB (MathWorks, Natick, MA, USA). The sharpness was obtained by calculating the quadratic sum of the partial derivative of the vessel image along x and y directions and then dividing it by the vessel length (34). Both vessel length and sharpness were calculated as dimensionless quantities. The degree of stenosis was measured based on the North American Symptomatic Carotid Endarterectomy Trial (NASCET) (35,36). Measurement of aneurysm involved the calculation of aneurysmal diameter according to the MIP reconstructions. The CTA or DSA was also acquired within 1 week after MRA for patients showing pathology.

Involved qualitative metrics were expressed as median and interquartile ranges. Quantitative variables were expressed as mean ± SD and ranges. Shapiro-Wilk test was conducted to check the normality of data distribution. Interobserver agreement was calculated using weighted Cohen's Kappa (37), in which values <0.4 represent poor agreement, values between 0.4 and 0.75 indicate fair to good agreement, and values >0.75 represent excellent agreement. Pairwise Wilcoxon test was used to evaluate the imaging quality derived from cTOF and sTOF acquisitions. The value $P<0.05$ indicated a statistically significant difference and all the tests were 2-sided. We used G*Power 3.1.9.7 to conduct statistical power analysis and determine the sample size. All other analyses were performed using MATLAB (version R2019a) and R software (version R 4.2.1; R Foundation for Statistical Computing, Vienna, Austria).

Results

Among the 37 initially recruited patients, 3 were excluded after initial selection according to our exclusion criteria (1 participant with severe motion artifact, 1 with inadequate imaging FOV, and 1 with other comorbidities). A total of 34 patients (55.79 years ±15.76; 18 women; 44.1% with pathology) who underwent cTOF followed by sTOF were finally recruited in our study. *Figure 1* shows the flowchart of patient recruitment. Of the 15 patients with intracranial vascular pathologies, 10 cases (66.7%) had stenosis (including 2 cases with occlusion), 4 cases (26.7%) had aneurysm, and 1 case (6.7%) had arteriovenous malformation. Among all the 17 lesions, 4 pathologies (23.5%) were at the ICA (2 at C5 segments and 2 at C6 segments), 4 pathologies (23.5%) were at the MCA (3 at M1 segments and 1 at M2 segment), 1 pathology (5.9%) at the BA, 2 pathologies (11.8%) at the V4 segments of VA, 2 pathologies (11.8%) at the P1 segment of PCA, 3 pathologies (17.6%) at the ACA (1 at A1 segment, 1 at A3 segment and 1 arteriovenous malformation), and 1 pathology (5.9%) at the anterior communicating artery (ACoA).

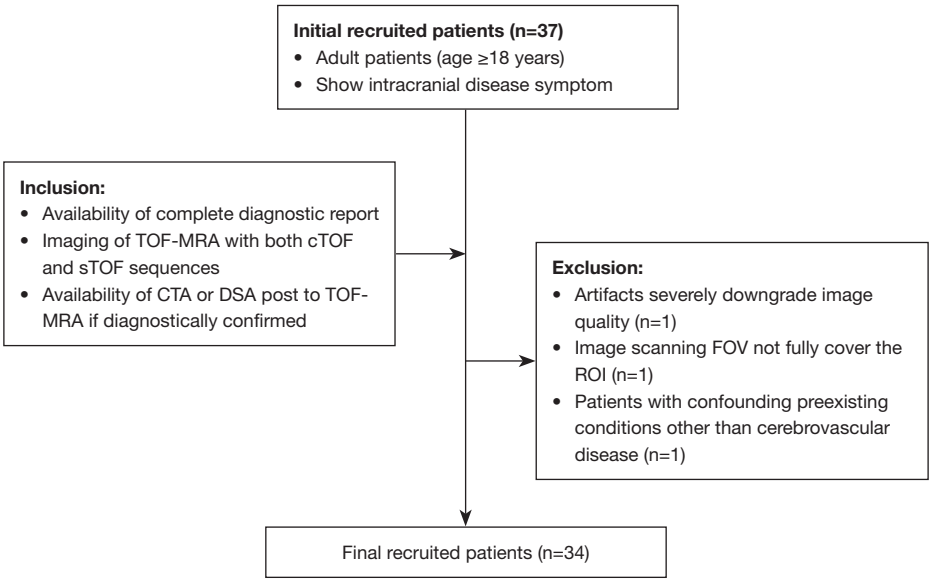

Figure 1 Flowchart of study cohort with exclusion criteria. FOV, field of view; ROI, region of interest; TOF-MRA, time-of-flight magnetic resonance angiography; cTOF, Cartesian-based TOF-MRA; sTOF, spiral based TOF-MRA; CTA, computed tomography angiography; DSA, digital subtraction angiography.

Comparison of original image quality

The original data of sTOF depicting arteries in the vicinity of the circle of Willis, collateral medium-sized and dispersed small vessels have shown distinctly better visualization in comparison to cTOF (*Figure 2*). The higher contrast and edge sharpness between vessels and periphery tissues are evidently presented with sTOF acquisition (*Figure 2A vs. Figure 2E* with left and right arteries in the vicinity of Willis circle), showing better visualization at the skull base. Additionally, sTOF is shown to be less affected by pulsatile artifacts commonly seen in cTOF (*Figure 2B vs. Figure 2F*, *Figure 2C vs. Figure 2G*). Besides, the rightmost column of *Figure 2* shows that when adjusting the acquisition resolution to the same isotropic 0.65 mm for both sequences, more tiny vessels would otherwise be neglected in cTOF are visible in sTOF (*Figure 2D vs. Figure 2H*).

Comparison of diagnostic efficacy

Lesion misdiagnosis

Table 2 summarizes qualitative assessment by 2 raters, which showed significant differences between sTOF and cTOF in most vessel segments and the weighted Cohen's Kappa ranged from 0.675 to 1. *Figure 3* depicts tough regions in presence of curved vessels. For the petrosal segment of the ICA (*Figure 3A* and *Figure 3E*, *Figure 3C* and *Figure 3G*, *Figure 3D* and *Figure 3H* with short arrows), the ocular segment of the ICA (*Figure 3B* and *Figure 3F* with short arrows), supra-cavernous sinus segment and clinoid segment of ICA (*Figure 3D* and *Figure 3H* with long arrows), loss of signals from vascular lumen may occur as a result of complex blood flow fluctuation. The cTOF after MIP reconstruction exhibited substantial pronounced false interruption of vascular continuity, which is susceptible to misdiagnosis as stenosis, occlusion, or disruption.

The overall assessment, as listed in *Table 3*, revealed that among all the false positive diagnosis cases of cTOF, 3 appeared at C2 segments of ICA, 1 appeared at C5 segment of ICA, 1 appeared at A1 segment of ACA, and 1 appeared at P1 segment of PCA. The cTOF was typically prone to overdiagnosis of the extent of stenosis, in which 1 case appeared at M1 segment of MCA, 1 case appeared at V4 segment of VA, and 1 case appeared at A1 segment of ACA. The sTOF is shown to better maintain the fidelity and be less prone to artifacts. Apart from the aforementioned intraosseous and intradural segments of ICA, better vessel morphology is also observed at skull base and vertebral arteries (*Figure 3* with circles), which would be helpful for patients with vertebrobasilar insufficiency.

Pathology imaging quality

For regions with pathologies, sTOF depicts lesions more

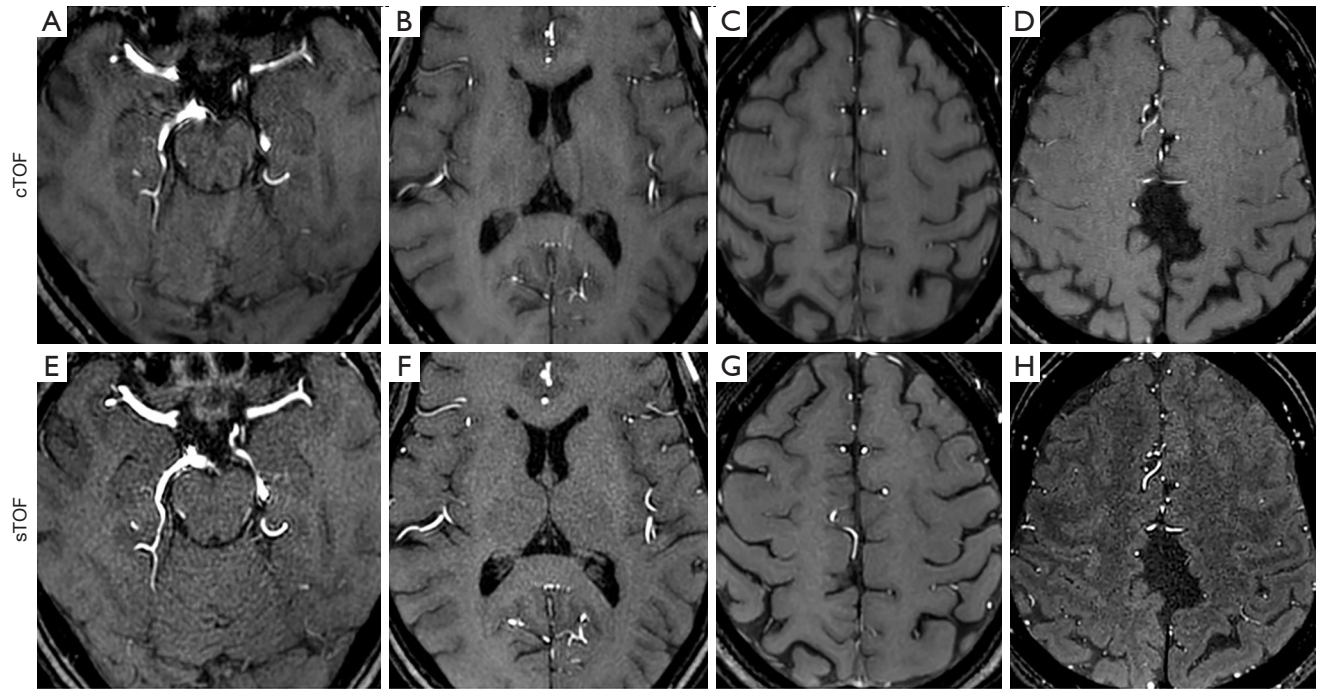

Figure 2 Raw data acquired from skull base till calvarium at different scales. The left 3 columns are data from the same patient with resolution of 0.8×0.8×1.2 mm^3, the resolution of the rightmost column is isotropic 0.65 mm. The above and bottom rows show respectively the original images of cTOF and sTOF. (A) and (E) depict left and right arteries in the vicinity of the circle of Willis; (B) and (F) depict collateral middle-sized arteries; (C,G) and (D,H) show interspersed small vessels. cTOF, Cartesian-based time-of-flight magnetic resonance angiography; sTOF, spiral-based time-of-flight magnetic resonance angiography.

Table 2 Qualitative vessel segment assessment

Vessel segment	cTOF		sTOF		P value
	Rater 1 score	Rater 2 score	Rater 1 score	Rater 2 score	
Extracranial ICA	5 (5, 5)	5 (5, 5)	5 (5, 5)	5 (5, 5)	>0.99
Intraosseous ICA	4 (3.75, 4)	4 (3, 4.25)	4 (4, 5)	5 (5, 5)	0.01
Intradural ICA	4 (3.75, 4)	4 (3.75, 4)	4 (4, 5)	4 (4.25, 4)	0.02
VA	5 (4, 5)	4 (3.75, 5)	5 (5, 5)	5 (5, 5)	0.02
BA	5 (4.75, 5)	5 (5, 5)	5 (5, 5)	5 (5, 5)	0.37
ACA	4.5 (3.75, 5)	4 (3.75, 4.25)	5 (4.75, 5)	5 (4.75, 5)	0.01
MCA	5 (4.75, 5)	5 (4.75, 5)	5 (5, 5)	5 (5, 5)	0.07
PCA	4.5 (4, 5)	4 (4, 4.25)	5 (4.75, 5)	5 (5, 5)	0.003
AchA	4 (2.75, 4)	3 (2.75, 3)	4 (3.75, 5)	4 (3, 4)	0.002
SCA	4 (4, 4)	3 (3, 3.25)	5 (4, 5)	5 (5, 5)	0.001
PCoA	3.5 (3, 4)	3 (3, 3.25)	4 (3.75, 4)	4 (3.75, 4)	0.006

Data are expressed as median [interquartile ranges (Q1, Q3)], P value: cTOF *vs.* sTOF. cTOF, Cartesian-based time-of-flight magnetic resonance angiography; sTOF, spiral-based time-of-flight magnetic resonance angiography; ICA, internal carotid artery; VA, vertebral artery; BA, basilar artery; ACA, anterior cerebral artery; MCA, middle cerebral artery; PCA, posterior cerebral artery; AchA, anterior choroidal artery; SCA, Superior cerebellar artery; PCoA, posterior communicating artery.

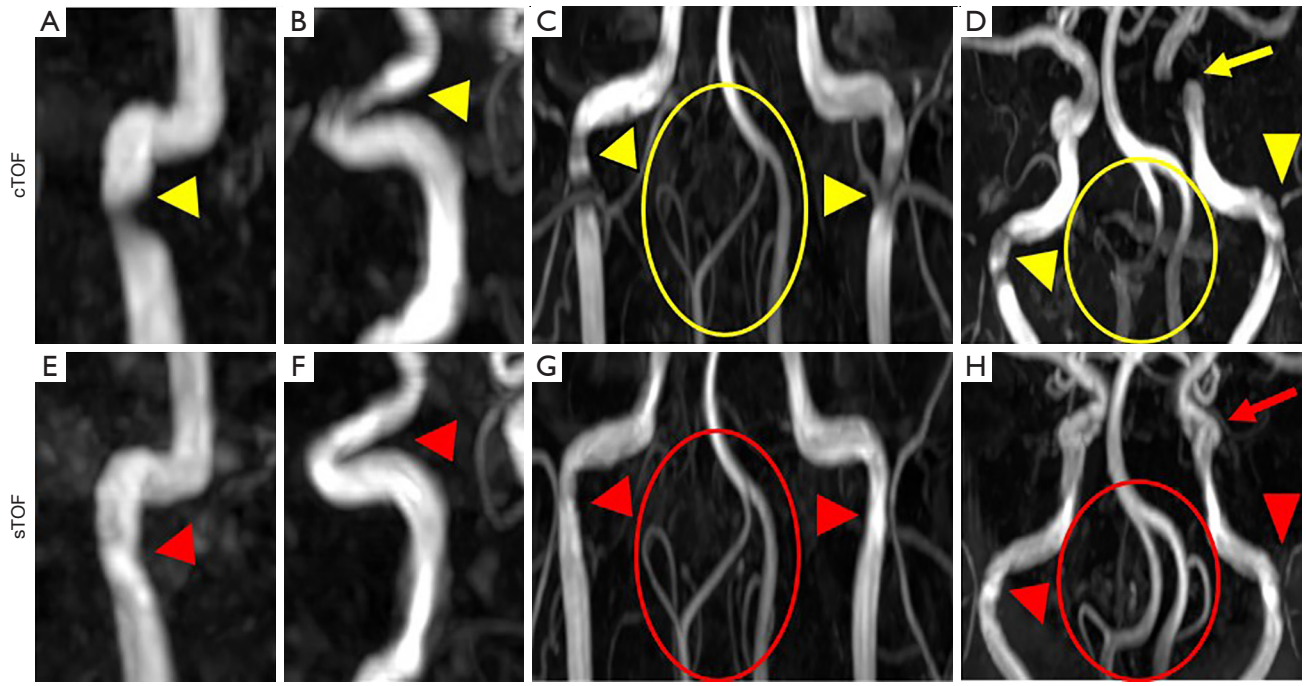

Figure 3 The above and bottom rows show respectively the MIP reconstruction of cTOF and sTOF. (A) and (E), (C) and (G) show the segment of petrosal bone; (B) and (F) show the ophthalmic and clinoid segment; (D) and (H) show the segment of petrosal bone while the long arrows show cavernous sinuses. Comparison reveals artifacts as false interruption of vascular continuity at different junctions for cTOF, where short arrows depict intraosseous segment of ICA (C2) and long arrows depict intradural segment of ICA (C4 and C5). Regions in circles show better visualization at skull base and vertebral arteries. cTOF, Cartesian-based time-of-flight magnetic resonance angiography; sTOF, spiral based time-of-flight magnetic resonance angiography; MIP, maximal intensity projection; ICA, internal carotid artery.

Table 3 List of incorrect diagnosis by cTOF

Pathologic region	Segment	Misdiagnosis type
ICA	C2	3 false positives
	C5	1 false positive
VA	V4	1 overdiagnosis
ACA	A1	1 false positive + 1 overdiagnosis
MCA	M1	1 overdiagnosis
PCA	P1	1 false positive

cTOF, Cartesian-based time-of-flight magnetic resonance angiography; ICA, internal carotid artery; VA, vertebral artery; ACA, anterior cerebral artery; MCA, middle cerebral artery; PCA, posterior cerebral artery.

clearly without inducing much ambiguity. The first column of *Figure 4* (*Figure 4A*,*4D*) shows microaneurysms at both sides of supra-cavernous sinus segments, whereas the signal of the right microaneurysm in cTOF is lower than that of sTOF. The sTOF depicts equally well and slightly better for aneurysms at the M1 bifurcation of the MCA, as shown in the middle 2 columns (*Figure 4B vs. Figure 4E*). Further, sTOF gives better visualization for big arteries with chronic atherosclerosis (*Figure 4C vs. Figure 4F*), showing its higher sensitivity to blood flow. The reduced artifacts can ease the diagnostic difficulty in distinguishing imaging artifacts from vessel plaque.

Quantitative comparisons and diagnostic reliability

Figure 5 shows quantitative comparisons of cTOF and sTOF regarding SNR, CNR, vessel length, and sharpness. We selected 4 typical regions, namely, the bilateral ACA, bilateral MCA, bilateral ICA, and BA, to evaluate the imaging qualities of both sequences. The sTOF was shown to excel cTOF in all regions without exception.

For images with occult vascular pathology, diagnosis was further validated via referral to CTA or DSA. The left

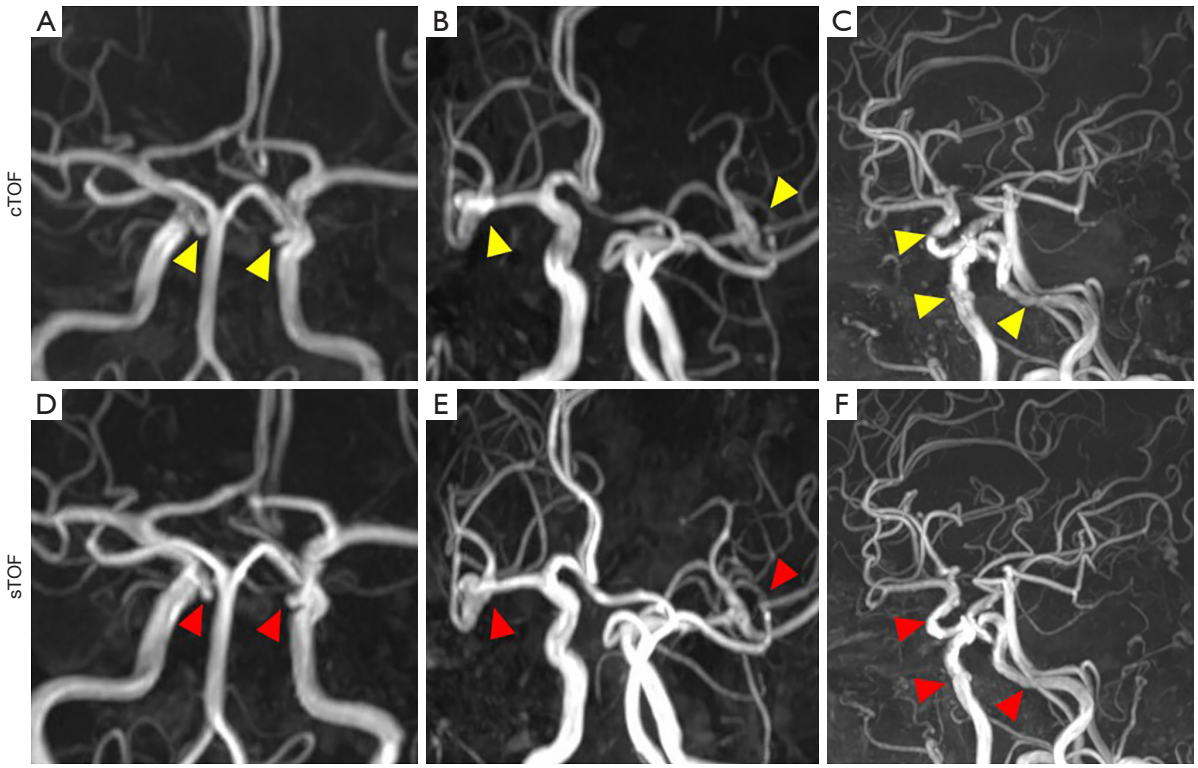

Figure 4 The above and bottom rows show respectively the MIP reconstruction of cTOF and sTOF. The arrows in the first column (A,D) show microaneurysms at both sides of supra-cavernous sinus segments. The arrows in the middle column (B,E) depict aneurysms at the M1 bifurcation of the middle cerebral artery. The right column (C,F) presents big arteries with chronic atherosclerosis, where the leftmost arrow depicts clinoid segment and the right 2 arrows depict foramen lacerum segment. cTOF, Cartesian-based time-of-flight magnetic resonance angiography; sTOF, spiral-based time-of-flight magnetic resonance angiography; MIP, maximal intensity projection.

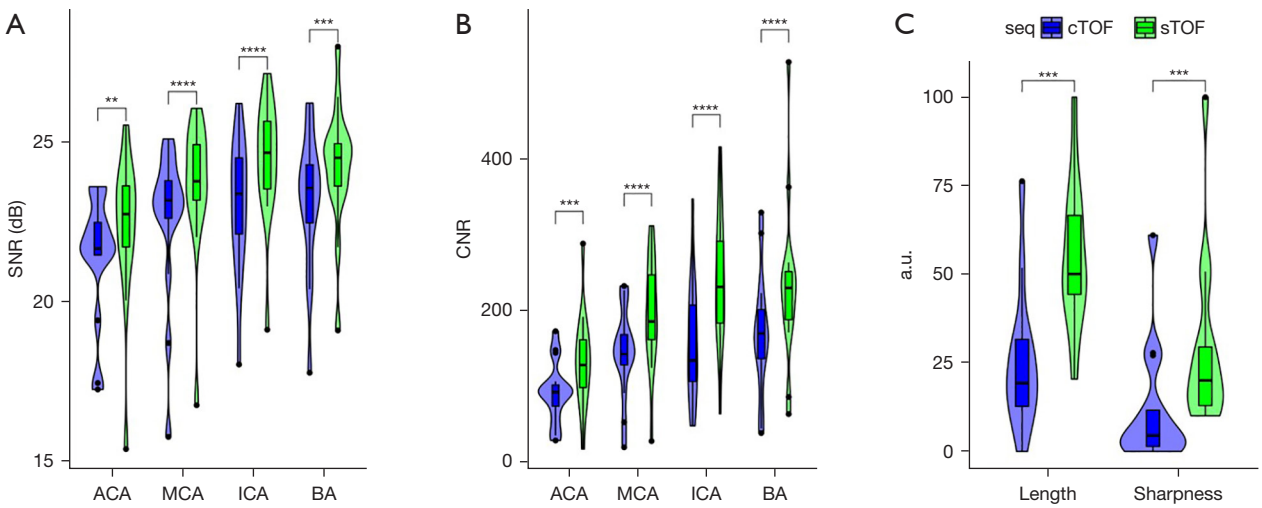

Figure 5 Quantitative comparisons of cTOF and sTOF regarding SNR (A), CNR (B), vessel length and sharpness (C) at selected ROIs such as bilateral ACA, bilateral MCA, bilateral ICA and BA. The asterisks show statistical significance between cTOF and sTOF, where **, ***, and **** respectively indicates P<0.01, P<0.001 and P<0.0001. SNR, signal-to-noise ratio; ACA, anterior cerebral artery; MCA, middle cerebral artery; ICA, internal carotid artery; BA, basilar artery; CNR, contrast-to-noise ratio; a.u., arbitrary unit; seq, sequence; cTOF, Cartesian-based time-of-flight magnetic resonance angiography; sTOF, spiral-based time-of-flight magnetic resonance angiography; ROI, region of interest.

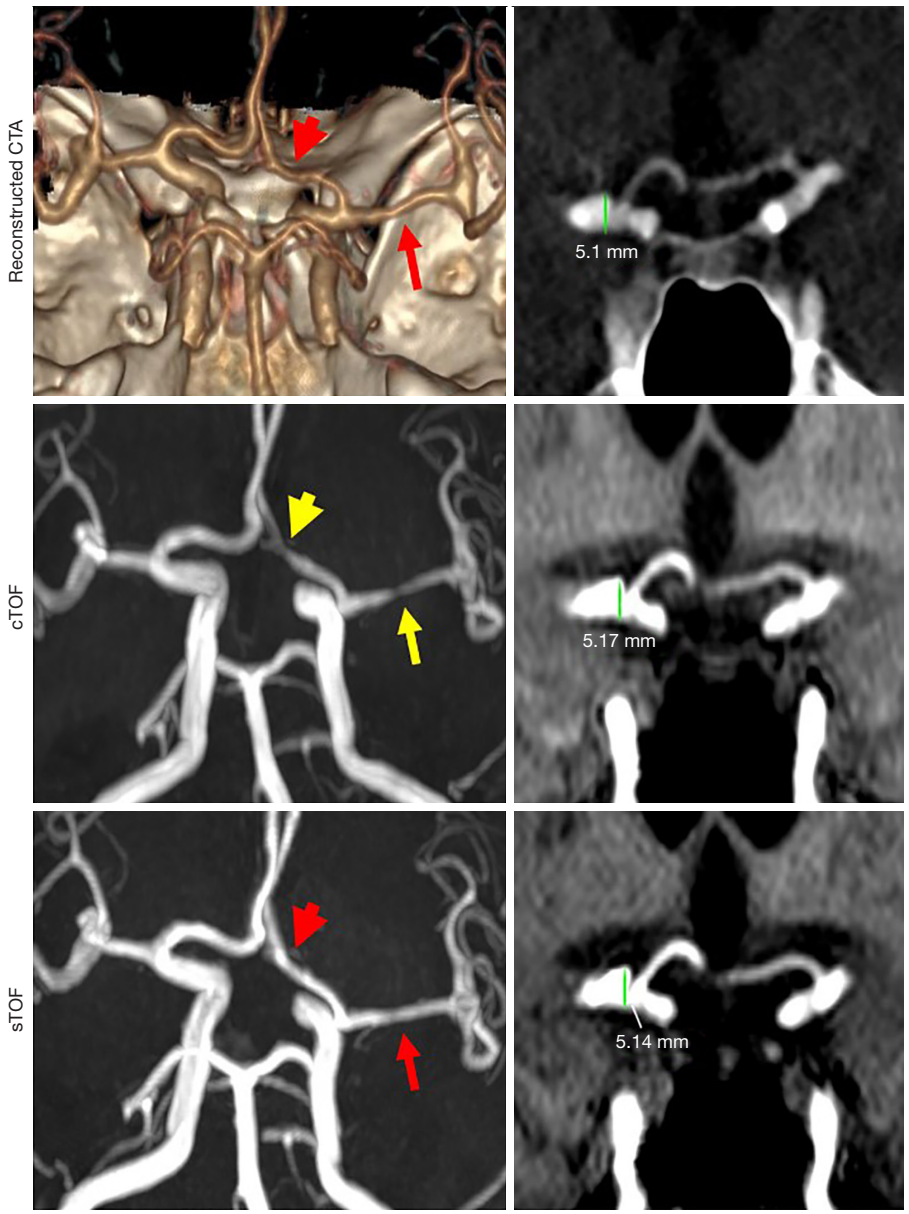

Figure 6 The above row shows reconstructed CTA, the middle and bottom rows show respectively the images of cTOF and sTOF. The left column shows the reliability of stenosis diagnosis at the A1 segment of ACA (short arrow) and the M1 segment of left MCA (long arrow). The right column depicts shape and size evaluation of aneurysm at the right proximal of MCA. CTA, computed tomography angiography; cTOF, Cartesian-based time-of-flight magnetic resonance angiography; sTOF, spiral-based time-of-flight magnetic resonance angiography; ACA, anterior cerebral artery; MCA, middle cerebral artery.

column of *Figure 6* shows stenosis at the A1 segment of ACA (short arrow) and the M1 segment of left MCA (long arrow) in cTOF. However, the extent of stenosis was overestimated after verification by CTA, and sTOF was shown to achieve a closer result to that of CTA measurement of vascular lumen iodide imaging. The right column of *Figure 6* depicts quantitative evaluation of a confirmed aneurysm at the right proximal of the MCA, revealing all sequences can obtain a consistent aneurysm size with acceptable deviation. The aneurysm assessment by cTOF and sTOF shows no

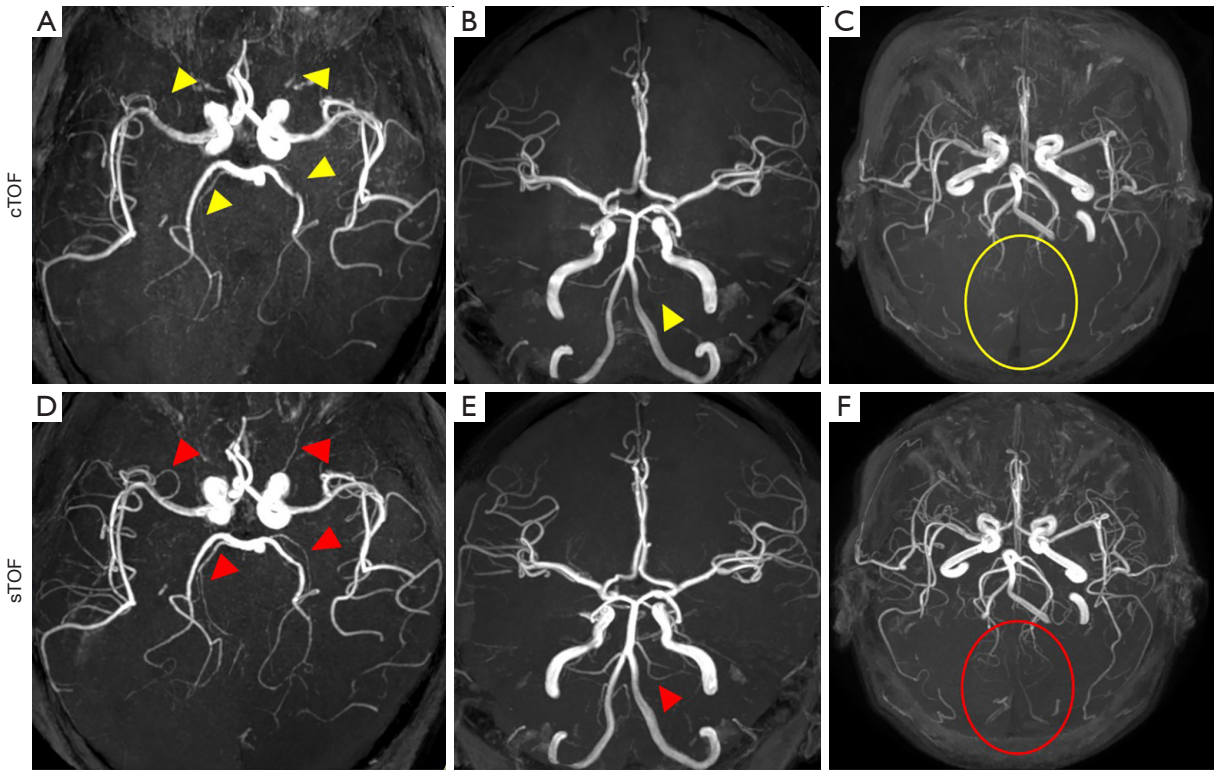

Figure 7 Distal vessel visualization. The above and bottom rows show respectively the MIP reconstruction of cTOF and sTOF. For (A) and (D), arrow on the top left depicts ophthalmic artery, arrow on the top right depicts middle cerebral artery branch, and the bottom two arrows show the inferior and superior PCA branches. For (B) and (E), arrows depict small vessels at basilar artery. For (C) and (F), circles depict the small vessels at P3 and P4 segments of PCA. cTOF, Cartesian-based time-of-flight magnetic resonance angiography; sTOF, spiral-based time-of-flight magnetic resonance angiography; MIP, maximal intensity projection; PCA, posterior cerebral artery.

significant size or shape difference (P>0.05).

Comparison of distal small vessels

Moreover, the centrally dense sampled spiral trajectories of sTOF can intrinsically compensate the effect of higher gradient moments in a more effective way as compared to cTOF, enabling an enhancement in CNR for small branch visualization. As shown in *Figure* 7, for *Figure* 7*A*,7*D*, the arrow on the top left depicts the ophthalmic artery, the arrow on the top right depicts the MCA branch, and the bottom 2 arrows show the inferior and superior PCA branches. Denser and detailed vessels of much smaller scales are shown at all these regions in sTOF. Both basilar and vertebral arteries are clearly displayed in *Figure* 7*E*, even tiny vessels at the BA are easily observable. Better visualization was obtained for small vessels at P3 and P4 segments of PCA, which would be difficult to display for cTOF (*Figure* 7*C vs. Figure* 7*F*).

Comparison of metal implant influence

For traumatic brain injury patients implanted with titanium plates (*Figure 8* long arrows) following cranioplasty, CTA and DSA examinations can be difficult as a result of X-ray absorption by the metal. The sTOF has been shown to maintain better resistance to magnetic susceptibility with higher SNR than that of cTOF (*Figure 8*). The top and middle arrows on the first column of *Figure 8* show that the farthest reachable distance of cTOF for the MCA was the branch of the anterior temporal artery, whereas sTOF was able to display both M1 and M2 segments. In addition, the bottom arrow shows that cTOF can only depict the proximal segment of the PCA, and the sTOF gives a better vascular profile.

Discussion

This study highlights the advantages of sTOF in

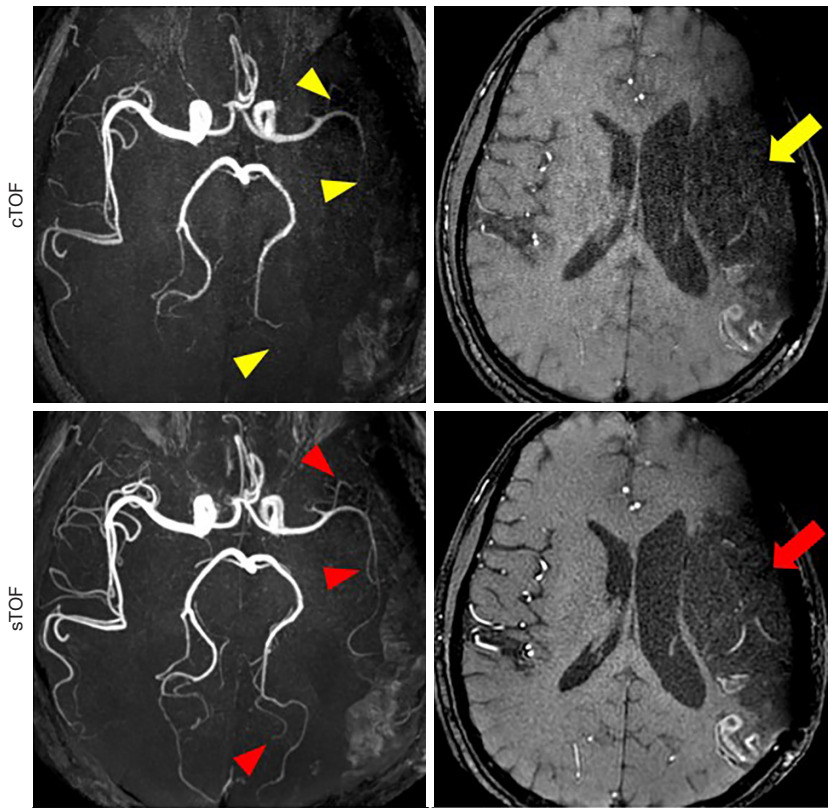

Figure 8 Patient with implanted titanium plate after cranioplasty. Short arrows depict comparisons of small vessel, and long arrows show the position where titanium plate was being implanted. cTOF, Cartesian-based time-of-flight magnetic resonance angiography; sTOF, spiral-based time-of-flight magnetic resonance angiography.

cerebrovascular MRA imaging. Compared to cTOF, the sTOF achieved better imaging quality and diagnostic efficacy. Analysis of pathologic regions showed its better resistance to false positive interpretation. The overall evaluation demonstrated the superiority of spiral acquired TOF-MRA image, highlighting sTOF as a competent surrogate of cTOF for routine imaging of intracranial vasculature.

In our study, we used a head/neck coil of 16 channels, as it is quite common and viable in practice for most of the hospitals. Higher performance is expected if we adopt a more elaborate coil, for example, with 32 channels. During the acquisition procedure, 3 minutes and 40 seconds was taken to acquire sTOF images with as many as 120 slices (FOV 180×180×120). Shortening the process is possible if fewer layers are scanned, or other parallel imaging techniques are adopted. Our experiments demonstrated that sTOF showed better imaging quality either for diagnosing intracranial lesions or depicting small vessels, even excelled at previously reported tough regions such as the skull base and intraosseous/intradural segments of the ICA (26), which was of clinical significance. The already-shown imaging capabilities have brought sTOF within the bounds of possibility to be used independently instead of bothering to utilize the complementary strength of both cTOF and sTOF to synergically obtain benefits from both sequences. Given the superiority of sTOF in displaying distal tiny vessels, it may facilitate the early diagnosis of small vessel-induced brain infarction, which has been reported to account for 20–25% of all ischemic stroke (5,38,39). Moreover, sTOF exhibits more tolerance toward intracranial metal implants, which will further expand its clinical usage given that various implants, such as endovascular stents or cranial titanium plates, can be commonly encountered in MR-related brain imaging.

Previous studies have shown that false positive interpretation may occur as a result of turbulent blood flow, or at regions with overlapping/-branching vasculatures, particularly for aneurysm detection at regions such as the ophthalmic artery, ACoA, anterior choroidal artery,

and relevant small branches of the ICA (30,40,41). Of note, sTOF can effectively mitigate artifacts and the influence of false-positive imaging prevalent in cTOF. For pathology detectability, aneurysms with diameters less than 5 mm are considered small and involve detection difficulties. Even though there have been studies reporting low rates in detecting small aneurysms, the false positives notably occurred due to vascular branching or vessels of infundibular shape; the better capability to display vascular details makes sTOF suitable for this task. Hence, at least for intracranial vessel imaging, the application of sTOF has brought spiral acquisition into the realm of feasibility in clinic routine.

TOF-MRA using spiral trajectory ensures good *k*-space sampling efficiency, and oversampling of central *k*-space makes it robust to resist artifacts even at a shorter scan duration. The intrinsically shorter echo time is directly associated with better SNR yield. The higher imaging quality of 3D spiral technique has expanded its multiple merits such as better spatiotemporal resolution and inherent self-calibration beyond conventional rectilinear acquisition. However, spiral readouts have rarely found a wide clinical application to date as it is typically impaired by the imperfection arising from inhomogeneous B_0 field, causing off-resonance effect with accumulated phase inaccuracy. The broadened or ring-shaped point spread function (PSF) and subsequent blurring or distortion require further correction. Moreover, spiral angiogram is also susceptible to the transient gradient perturbations including bulk motion, dynamic susceptibility, magnet drifts, concomitant fields, eddy currents, and so on, which will also lead to image blurring and other artifacts particularly within close vicinity of skull or at tissue-air interfaces. Our MRA imaging is fat suppressed, so it can better resist chemical shift artifacts. The susceptibility effect can be mitigated by adjusting a relatively short sampling window. The blurring caused by off-resonance is usually corrected during the reconstruction process based on the magnetic field map obtained prior to the spiral scan. Recent solutions have involved the inversion of expanded encoding model including static off-resonance maps, concurrent field monitoring, and coil sensitivity information with iterative reconstruction (42). Another approach sought to model the behavior of the gradient chain via gradient impulse response function to correct *k*-space trajectory deviation. Deep learning-based correction schemes will also be a suitable candidate to overcome the above-mentioned obstacles.

Our study had limitations. Firstly, the relatively small cohort we have so far enrolled within 1 clinic site may potentially have led to bias being caused during the evaluation process. It is imperative to confirm the feasibility by recruiting larger quantities incorporation of multicenter datasets. Secondly, the advantages of sTOF have so far not been sufficiently explored, especially the foreseeable superiority of optimized sTOF acquisition. Although sTOF is flexible to be extended to imaging other parts of the body, we have not implemented it in regions other than brain vasculature. It is promising to apply sTOF to other tough regions to further reveal it's advantages. More in-depth assessment of diagnostic performance can be focused on specific vascular syndromes. Comparisons with other noninvasive acquisition methods, for example, ASL-based MRA or application on clipped aneurysm (43), will be well worth further exploration. Lastly, if optimizing sTOF to accelerate the imaging procedure by, for example, multi-slice excitation or other parallel reconstruction strategies, we would anticipate an improved acquisition performance that can better freeze fluid-induced artifacts as well as shorten the scanning duration for patients with acute onset of cerebrovascular disease.

Conclusions

The sTOF acquisition offers comparatively better imaging quality than the standard Cartesian-based cTOF sequence. The majority of clinical trials have evaluated and emphasized the complementary benefits of spiral imaging as to Cartesian TOF-MRA. Based on our results, sTOF can be independently applied to derive an angiogram suitable for intracranial pathological diagnosis. The achieved performances shed light on its competence over the Cartesian-based method and the possibility to become a formal TOF-MRA acquisition protocol for future cerebral angiography. Even more noteworthy is that by integrating spiral intrinsic merits and other parallel imaging strategies, sTOF has much potential to be further optimized. These advantages may facilitate an expanded clinical and investigative application of sTOF to aid cerebrovascular disease management with convenient and non-invasive implementation.

Acknowledgments

Funding: This study was supported by the National Natural Science Foundation of China (No. 82102021, No. 82071913, and No. 22161142024); the Postdoctoral

Research Foundation of China (No. 2020M671947); and the Doctoral Scientific Research Foundation (No. 2023BSZR011).

Footnote

Reporting Checklist: The authors have completed the STROBE reporting checklist. Available at https://qims.amegroups.com/article/view/10.21037/qims-23-1533/rc

Conflicts of Interest: All authors have completed the ICMJE uniform disclosure form (available at https://qims.amegroups.com/article/view/10.21037/qims-23-1533/coif). L.X. reports this study was supported by the National Natural Science Foundation of China (No. 82102021), the Postdoctoral Research Foundation of China (No. 2020M671947), and the Doctoral Scientific Research Foundation (No. 2023BSZR011). L.L. reports that he is an MR collaborating scientist from Philips Healthcare providing technical support under the Philips collaboration regulations and has no financial or other conflicts for this study. C.C. reports that this study was supported by the National Natural Science Foundation of China (No. 82071913). Z.C. reports that this study was supported by the National Natural Science Foundation of China (No. 22161142024). The other authors have no conflicts of interest to declare.

Ethical Statement: The authors are accountable for all aspects of the work in ensuring that questions related to the accuracy or integrity of any part of the work are appropriately investigated and resolved. The study was conducted in accordance with the Declaration of Helsinki (as revised in 2013). The study was approved by the Institutional Review Board of Zhongshan Hospital of Xiamen University (No. xmzsyyky[2019019]) with written informed consent provided by all individual participants.

References

1. Simonds GR, Truwit CL. Anatomy of the cerebral vasculature. Neuroimaging Clin N Am 1994;4:691-706.
2. Salehi A, Zhang JH, Obenaus A. Response of the cerebral vasculature following traumatic brain injury. J Cereb Blood Flow Metab 2017;37:2320-39.
3. Blair GW, Thrippleton MJ, Shi Y, Hamilton I, Stringer M, Chappell F, Dickie DA, Andrews P, Marshall I, Doubal FN, Wardlaw JM. Intracranial hemodynamic relationships in patients with cerebral small vessel disease. Neurology 2020;94:e2258-69.
4. Anzalone N, Scomazzoni F, Strada L, Patay Z, Scotti G. Intracranial vascular malformations. Eur Radiol 1998;8:685-90.
5. Behrouz R, Malek AR, Torbey MT. Small vessel cerebrovascular disease: the past, present, and future. Stroke Res Treat 2012;2012:839151.
6. Krishnamurthi RV, Ikeda T, Feigin VL. Global, Regional and Country-Specific Burden of Ischaemic Stroke, Intracerebral Haemorrhage and Subarachnoid Haemorrhage: A Systematic Analysis of the Global Burden of Disease Study 2017. Neuroepidemiology 2020;54:171-9.
7. Yang Y, Rosenberg GA. Blood-brain barrier breakdown in acute and chronic cerebrovascular disease. Stroke 2011;42:3323-8.
8. Manninen AL, Isokangas JM, Karttunen A, Siniluoto T, Nieminen MT. A comparison of radiation exposure between diagnostic CTA and DSA examinations of cerebral and cervicocerebral vessels. AJNR Am J Neuroradiol 2012;33:2038-42.
9. van Asch CJ, Velthuis BK, Rinkel GJ, Algra A, de Kort GA, Witkamp TD, et al. Diagnostic yield and accuracy of CT angiography, MR angiography, and digital subtraction angiography for detection of macrovascular causes of intracerebral haemorrhage: prospective, multicentre cohort study. BMJ 2015;351:h5762.
10. Bosch de Basea Gomez M, Thierry-Chef I, Harbron R, Hauptmann M, Byrnes G, Bernier MO, et al. Risk of hematological malignancies from CT radiation exposure in children, adolescents and young adults. Nat Med 2023;29:3111-9.
11. Kaufmann TJ, Huston J 3rd, Mandrekar JN, Schleck CD, Thielen KR, Kallmes DF. Complications of diagnostic cerebral angiography: evaluation of 19,826 consecutive patients. Radiology 2007;243:812-9.
12. Lin A, Rawal S, Agid R, Mandell DM. Cerebrovascular

Imaging: Which Test is Best? Neurosurgery 2018;83:5-18.
13. Willinsky RA, Taylor SM, TerBrugge K, Farb RI, Tomlinson G, Montanera W. Neurologic complications of cerebral angiography: prospective analysis of 2,899 procedures and review of the literature. Radiology 2003;227:522-8.
14. Grossberg JA, Howard BM, Saindane AM. The use of contrast-enhanced, time-resolved magnetic resonance angiography in cerebrovascular pathology. Neurosurg Focus 2019;47:E3.
15. Anzalone N. Contrast-enhanced MRA of intracranial vessels. Eur Radiol 2005;15 Suppl 5:E3-10.
16. Bock J, Frydrychowicz A, Stalder AF, Bley TA, Burkhardt H, Hennig J, Markl M. 4D phase contrast MRI at 3 T: Effect of standard and blood-pool contrast agents on SNR, PC-MRA, and blood flow visualization. Magn Reson Med 2010;63:330-8.
17. Fall S, Pagé G, Bettoni J, Bouzerar R, Balédent O. Use of Phase-Contrast MRA to Assess Intracranial Venous Sinus Resistance to Drainage in Healthy Individuals. AJNR Am J Neuroradiol 2017;38:281-7.
18. Koktzoglou I, Huang R, Edelman RR. Quantitative time of flight MR angiography for simultaneous luminal and hemodynamic evaluation of the intracranial arteries. Magn Reson Med 2021;87:150-62.
19. Urbach H, Dorenbeck U, von Falkenhausen M, Wilhelm K, Willinek W, Schaller C, Flacke S. Three-dimensional time-of-flight MR angiography at 3 T compared to digital subtraction angiography in the follow-up of ruptured and coiled intracranial aneurysms: a prospective study. Neuroradiology 2008;50:383-9.
20. Sohn CH, Sevick RJ, Frayne R. Contrast-enhanced MR angiography of the intracranial circulation. Magn Reson Imaging Clin N Am 2003;11:599-614.
21. Miki H. Pitfalls in diagnosing cerebrovascular diseases using magnetic resonance angiography. Brain Nerve 2010;62:477-88.
22. Sailer AM, Wagemans BA, Nelemans PJ, de Graaf R, van Zwam WH. Diagnosing intracranial aneurysms with MR angiography: systematic review and meta-analysis. Stroke 2014;45:119-26.
23. Dhundass S, Savatovsky J, Duron L, Fahed R, Escalard S, Obadia M, Zuber K, Metten MA, Mejdoubi M, Blanc R, Sadik JC, Collin A, Lecler A. Improved detection and characterization of arterial occlusion in acute ischemic stroke using contrast enhanced MRA. J Neuroradiol 2020;47:278-83.
24. Raghuram A, Patel R, Varon A, Sabotin R, Sanchez S, Derdeyn CP, Jabbour P, Hasan DM, Samaniego EA. Volumetric surveillance of brain aneurysms: Pitfalls of MRA. Interv Neuroradiol 2023;29:532-9.
25. Yeh EN, Stuber M, McKenzie CA, Botnar RM, Leiner T, Ohliger MA, Grant AK, Willig-Onwuachi JD, Sodickson DK. Inherently self calibrating non-cartesian parallel imaging. Magn Reson Med 2005;54:1-8.
26. Greve T, Sollmann N, Hock A, Hey S, Gnanaprakasam V, Nijenhuis M, Zimmer C, Kirschke JS. Highly accelerated time-of-flight magnetic resonance angiography using spiral imaging improves conspicuity of intracranial arterial branches while reducing scan time. Eur Radiol 2020;30:855-65.
27. Greve T, Sollmann N, Hock A, Zimmer C, Kirschke JS. Novel Ultrafast Spiral Head MR Angiography Compared to Standard MR and CT Angiography. J Neuroimaging 2021;31:45-56.
28. Sartoretti E, Sartoretti-Schefer S, van Smoorenburg L, Binkert CA, Schwenk Á, Gutzeit A, Mannil M, Wyss M, Sartoretti T. Contrast-Enhanced T1-Weighted Head and Neck MRI: Prospective Intraindividual Image Quality Comparison of Spiral GRE, Cartesian GRE, and Cartesian TSE Sequences. AJR Am J Roentgenol 2022;218:132-9.
29. Sartoretti T, Sartoretti E, Schwenk Á, van Smoorenburg L, Mannil M, Euler A, Becker AS, Alfieri A, Najafi A, Binkert CA, Wyss M, Sartoretti-Schefer S. Clinical feasibility of ultrafast intracranial vessel imaging with non-Cartesian spiral 3D time-of-flight MR angiography at 1.5T: An intra-individual comparison study. PLoS One 2020;15:e0232372.
30. Nedim KA, Vural A. Fast three-dimensional time-of-flight magnetic resonance angiography: Should it be used in routine neuroimaging for headaches? Int J Health Sci (Qassim) 2021;15:28-33.
31. Sartoretti T, van Smoorenburg L, Sartoretti E, Schwenk Á, Binkert CA, Kulcsár Z, Becker AS, Graf N, Wyss M, Sartoretti-Schefer S. Ultrafast Intracranial Vessel Imaging With Non-Cartesian Spiral 3-Dimensional Time-of-Flight Magnetic Resonance Angiography at 1.5 T: An In Vitro and Clinical Study in Healthy Volunteers. Invest Radiol 2020;55:293-303.
32. Shi Z, Zhao X, Zhu S, Miao X, Zhang Y, Han S, Wang B, Zhang B, Ye X, Dai Y, Chen C, Rao S, Lin J, Zeng M, Wang H. Time-of-Flight Intracranial MRA at 3 T versus 5 T versus 7 T: Visualization of Distal Small Cerebral Arteries. Radiology 2023;306:207-17.
33. Pruessmann KP, Weiger M, Scheidegger MB, Boesiger P. SENSE: sensitivity encoding for fast MRI. Magn Reson

Med 1999;42:952-62.
34. Katoh M, Stuber M, Buecker A, Günther RW, Spuentrup E. Spin-labeling coronary MR angiography with steady-state free precession and radial k-space sampling: initial results in healthy volunteers. Radiology 2005;236:1047-52.
35. Bash S, Villablanca JP, Jahan R, Duckwiler G, Tillis M, Kidwell C, Saver J, Sayre J. Intracranial vascular stenosis and occlusive disease: evaluation with CT angiography, MR angiography, and digital subtraction angiography. AJNR Am J Neuroradiol 2005;26:1012-21.
36. Samuels OB, Joseph GJ, Lynn MJ, Smith HA, Chimowitz MI. A standardized method for measuring intracranial arterial stenosis. AJNR Am J Neuroradiol 2000;21:643-6.
37. Fleiss JL, Levin B, Paik MC. Statistical Methods for Rates and Proportions. 3rd ed John Wiley; Sons, Inc., 2003.
38. Pantoni L. Cerebral small vessel disease: from pathogenesis and clinical characteristics to therapeutic challenges. Lancet Neurol 2010;9:689-701.
39. Petty GW, Brown RD Jr, Whisnant JP, Sicks JD, O'Fallon WM, Wiebers DO. Ischemic stroke subtypes : a population-based study of functional outcome, survival, and recurrence. Stroke 2000;31:1062-8.
40. Lu H, Nagae-Poetscher LM, Golay X, Lin D, Pomper M, van Zijl PC. Routine clinical brain MRI sequences for use at 3.0 Tesla. J Magn Reson Imaging 2005;22:13-22.
41. Schwab KE, Gailloud P, Wyse G, Tamargo RJ. Limitations of magnetic resonance imaging and magnetic resonance angiography in the diagnosis of intracranial aneurysms. Neurosurgery 2008;63:29-34; discussion 34-5.
42. Wilm BJ, Barmet C, Gross S, Kasper L, Vannesjo SJ, Haeberlin M, Dietrich BE, Brunner DO, Schmid T, Pruessmann KP. Single-shot spiral imaging enabled by an expanded encoding model: Demonstration in diffusion MRI. Magn Reson Med 2017;77:83-91.
43. Katsuki M, Narita N, Ishida N, Sugawara K, Watanabe O, Ozaki D, Sato Y, Kato Y, Jia W, Tominaga T. Usefulness of 3 Tesla Ultrashort Echo Time Magnetic Resonance Angiography (UTE-MRA, SILENT-MRA) for Evaluation of the Mother Vessel after Cerebral Aneurysm Clipping: Case Series of 19 Patients. Neurol Med Chir (Tokyo) 2021;61:193-203.

Cite this article as: Xu L, Wu J, Kang T, Lin L, Lv S, Lin J, Feng Z, Cai C, Chen Z. Spiral time-of-flight magnetic resonance angiography for intracranial vascular imaging: performance compared to conventional Cartesian angiogram. Quant Imaging Med Surg 2024;14(5):3417-3431. doi: 10.21037/qims-23-1533

